

THEORETICAL LIMB DARKENING FOR PULSATING CEPHEIDS

MASSIMO MARENGO, DIMITAR D. SASSELOV, MARGARITA KAROVSKA, AND COSTAS PAPALIOIOS

Harvard-Smithsonian Center for Astrophysics, 60 Garden Street, Cambridge, MA 02138; mmarengo@cfa.harvard.edu, dsasselov@cfa.harvard.edu, mkarovska@cfa.harvard.edu, cpapaliolos@cfa.harvard.edu

AND

J. T. ARMSTRONG

Remote Sensing Division, Naval Research Laboratory, Code 7210, Washington, DC 20375; tarmstr@gemini.usno.navy.mil

Received 2001 August 20; accepted 2001 November 14

ABSTRACT

Ground-based interferometry has finally reached a stage in which accurate determination of Cepheid diameters using the Baade-Wesselink method is feasible. Determining these diameters is the basis for calibrating the period-luminosity relation for classical Cepheids, and thus the extragalactic distance scale, but requires accurate limb-darkened models. This work presents a new method to compute time- and wavelength-dependent center-to-limb brightness distributions for classical Cepheids. Our model atmospheres are based on second-order accurate one-dimensional hydrodynamic calculations performed in spherical geometry. The brightness intensity distributions and the resulting limb darkening are computed through the dynamic atmospheres by using a full set of atomic and molecular opacities. Our results confirm important differences with respect to equivalent hydrostatic models. The amount of limb darkening and the shape of the limb profiles show a strong dependence on the pulsational phase of the Cepheid, which cannot be reproduced by static models. Nonlinear effects in our hydrodynamic equations add a new level of complexity in the wavelength dependence of our limb profiles, which are affected by the presence of shock waves traveling through the atmosphere. These effects, already detectable by present-day interferometers, should be taken into consideration when deriving limb-darkened diameters for nearby Cepheids with the accuracy required to measure their radial pulsations.

Subject headings: Cepheids — stars: atmospheres — stars: oscillations — techniques: interferometric

1. INTRODUCTION

Classical Cepheids play a central role in setting the extragalactic distance scale. In fact, Cepheid high intrinsic luminosity, and the existence of a well-studied relation between their pulsation period and luminosity (first discovered by Leavitt 1906), makes them crucial primary distance indicators. These properties have been exploited extensively, from early surveys to the recently completed *Hubble Space Telescope* Key Project to measure the Hubble constant (Freedman et al. 2001).

The reliability of Cepheids as distance indicators depends on the accurate calibration of the period-luminosity relation zero point. This is difficult to accomplish, owing to the low-density distribution of Cepheids in our Galaxy. Direct determination of the trigonometric parallaxes of the nearest Cepheids has been attempted using the database of the *Hipparcos* mission (see, e.g., Feast & Catchpole 1997), but large errors do not allow an unambiguous interpretation of the results (Madore & Freedman 1998). An accurate measurement of the parallaxes of even the closest Galactic Cepheids does not appear feasible, even with the space-based surveys proposed for the near future (Horner et al. 2000). Most promising among the techniques that can provide an independent calibration of the period luminosity zero point is the Baade-Wesselink (BW) method (Baade 1926; Wesselink 1946).

Recent progress in ground-based interferometry finally allows direct detection of pulsations in nearby Cepheids (Lane et al. 2000). The measurement of such radial angular variations, combined with spectroscopic observations yielding the radial velocity of the pulsating photosphere, can in principle allow a precise determination of nearby Cepheid distances (Sasselov & Karovska 1994, hereafter SK94). As

described in SK94, the feasibility of such a measurement is conditioned on the availability of accurate hydrodynamic models for the Cepheid atmospheres. These are required (1) to derive the projection factor necessary to convert the photospheric line velocities into radial motion and (2) to compute reliable time-dependent limb-darkening profiles. The first of these requirements is described in SK94 and addressed in detail by Sabbey et al. (1995). In this paper we describe a new approach to solve the second of these requirements.

Currently, limb-darkening tables specifically computed for Cepheid atmospheres are not available, so coefficients derived for static atmospheres of nonvariable yellow supergiants are generally used (Parsons 1971; Manduca, Bell, & Gustafsson 1977; Manduca 1979; Kurucz 1993a; Claret et al. 1995). This follows the assumption that a Cepheid atmosphere at a given phase can be approximated with a static plane-parallel atmosphere having the same T_{eff} and $\log g$, as estimated by fitting the depth ratio of weak photospheric lines. This is generally true as long as the observational constraints do not demand a level of precision that is affected by the time-dependent hydrodynamics and by the spherical geometry of the real pulsating star.

The assumptions of hydrostatic equilibrium and plane parallel geometry lead to an underestimation of the temperature gradients in yellow supergiants and thus fail to reproduce the correct IR and UV fluxes (Fieldus & Lester 1990). They also cannot reproduce the relative separation between the continuum photosphere and the line-forming region and thus underestimate the difference in the radial velocity amplitudes (Karp 1975; Sasselov & Raga 1992). All these and other limitations of static plane-parallel atmospheres seriously affect the precision of Cepheid distance

determination with the BW method. Current demands on a Cepheid distance scale accuracy of 10% and better require us to abandon the approximation of hydrostatic equilibrium and plane-parallel geometry (see SK94).

In Sasselov & Lester (1994), new time-dependent, non-LTE dynamic models of classical Cepheids were presented, and Sabbey et al. (1995) used them to study spectral line formation. In our paper, updated models are used to further explore the consequences of the dynamic treatment of Cepheid pulsation in the resulting spectral brightness distribution and limb profiles. This last step is complex since a consistent model, able to treat at the same time non-LTE radiative transfer and spherical geometry with all the necessary opacities and line sources in a time-dependent hydrodynamic framework, is still not feasible. Section 2 illustrates our solution to this problem.

In § 3 the typical results for a classical Cepheid are analyzed, and the differences between our computed limb-darkened profile and the one from an equivalent static atmosphere are discussed. The wavelength dependence of our limb profiles is also analyzed. In § 4 we finally discuss the applications of our models and their implication on the analysis of presently available and future interferometric measurements.

2. SPECTRAL INTENSITIES FOR DYNAMIC ATMOSPHERES

The computation of a realistic spectral intensity distribution for a stellar model requires a complete set of opacities for the atmospheric atomic species. If $T_{\text{eff}} \lesssim 7000$ K (which is generally true for classical Cepheids), molecules should also be included. Ideally, this requires solving the full radiative transfer problem and the hydrodynamic equations in a self-consistent way. However, the needed computing power is excessive, and therefore the hydrodynamic structure of the atmosphere is computed by considering only a limited set of elements (see discussion in § 2.1). The full set of elements and their opacities should somehow be reintroduced when deriving the emergent spectra.

A possible approach consists in using the Rosseland opacities derived in hydrostatic equilibrium. The hydrostatic equivalent of the dynamic model is chosen to match as close as possible the dynamic atmosphere, as it changes during the Cepheid pulsation. For each snapshot of the hydrodynamic simulation, one has to search for a static LTE model producing the same total flux of the star and having a similar atmospheric structure. A “hybrid” model is thus artificially constructed, having the depth-dependent opacities of the static atmosphere and the temperature, electron density, and pressure of the dynamic model atmosphere.

The main limitation of this procedure is that the opacities are still computed in LTE conditions. However, the intensity distributions thus derived are much improved, since the thermodynamical state is set by the hydrodynamic calculations. The accuracy and caveats of this technique are analyzed and discussed in the following sections.

2.1. Dynamic Models

Hydrodynamic simulations show fundamental departures in the structure of pulsating atmospheres from hydrostatic equilibrium and LTE (Willson & Bowen 1985; Cuntz 1987). Our hydrodynamic calculations only include model ions of H, He I and II, Ca II, and Mg II (see Sasselov & Lester 1994 for details). Additional non-LTE calculations are then

performed with model ions of C I and II, O I, Mg I, Ca I, and Fe I. These additional species do not provide any feedback for the radiative hydrodynamic simulations and are thus considered only for the starting models, and after the dynamic calculations have converged. For Galactic Cepheids, solar composition is assumed for all elements.

The pulsation is introduced by perturbing the atmosphere with a “piston” having suitable period, amplitude, and shape. These parameters are specific for each Cepheid under study and are derived from observational constraints. The period of the piston is the period of the Cepheid. The shape of the piston is taken from the linear nonadiabatic model computations of Buchler, Moskalik, & Kovacs (1990). The piston amplitude is the main free parameter and is derived by matching the radial velocity curve, the phase lags, the estimated extension of the atmosphere, the observed color and light variations, and other basic observable features. When the oscillations introduced by the piston stabilize and no transients remain, a set of time-dependent pulsating photospheric models are computed for the entire pulsational cycle. The details of this procedure are explained in Sasselov & Lester (1994).

Given a good model for the Cepheid piston, it is thus possible to fit the main stellar observables with a set of dynamic models, each one representing a snapshot of the atmosphere at any pulsational phase. We have applied this procedure for ζ Gem, which is a typical classical Cepheid.

We note that in Sasselov & Lester (1994) a further step is performed, which consists of building a semiempirical chromosphere to derive the phase-dependent profile of individual chromospheric lines. Since we are mostly interested in deriving low spectral resolution intensities and visibilities, the computed chromosphere is ignored in this work, owing to its negligible contribution to the overall limb-darkening profiles.

2.2. Dynamic Models and Stellar Observables

The Cepheid pulsation leads to the extension and contraction of the atmosphere, responsible for the changes of the stellar observables (T_{eff} , photospheric line velocity, radius, luminosity, etc.). These quantities, which change with the phase of a pulsating star, parameterize the computation of its phase-dependent spectrum. Let us define a consistent reference framework for the phases of a Cepheid cycle.

Traditionally, the zero-point phase of variable stars is set to coincide with maximum luminosity. This choice, however, is not convenient when dealing with time-dependent hydrodynamic models, since the emergent flux in the visible is a derived quantity, not always available in the numerical computation. A better approach is to use hydrodynamic quantities directly related to observables. The common choice is the pulsational velocity of the Cepheid photosphere, which can be observed by measuring the Doppler shift of suitable photospheric lines.

Figure 1 (*left*) shows the radial velocity and light curve of ζ Gem. These were derived by tables published by Bersier et al. (1994a, 1994b), where these parameters are measured for a large set of Cepheids and expressed in terms of their Fourier coefficients. The conversion of radial velocities into pulsational motion requires us to perform the following geometric transformation:

$$v_p \simeq -p(v_r - \gamma), \quad (1)$$

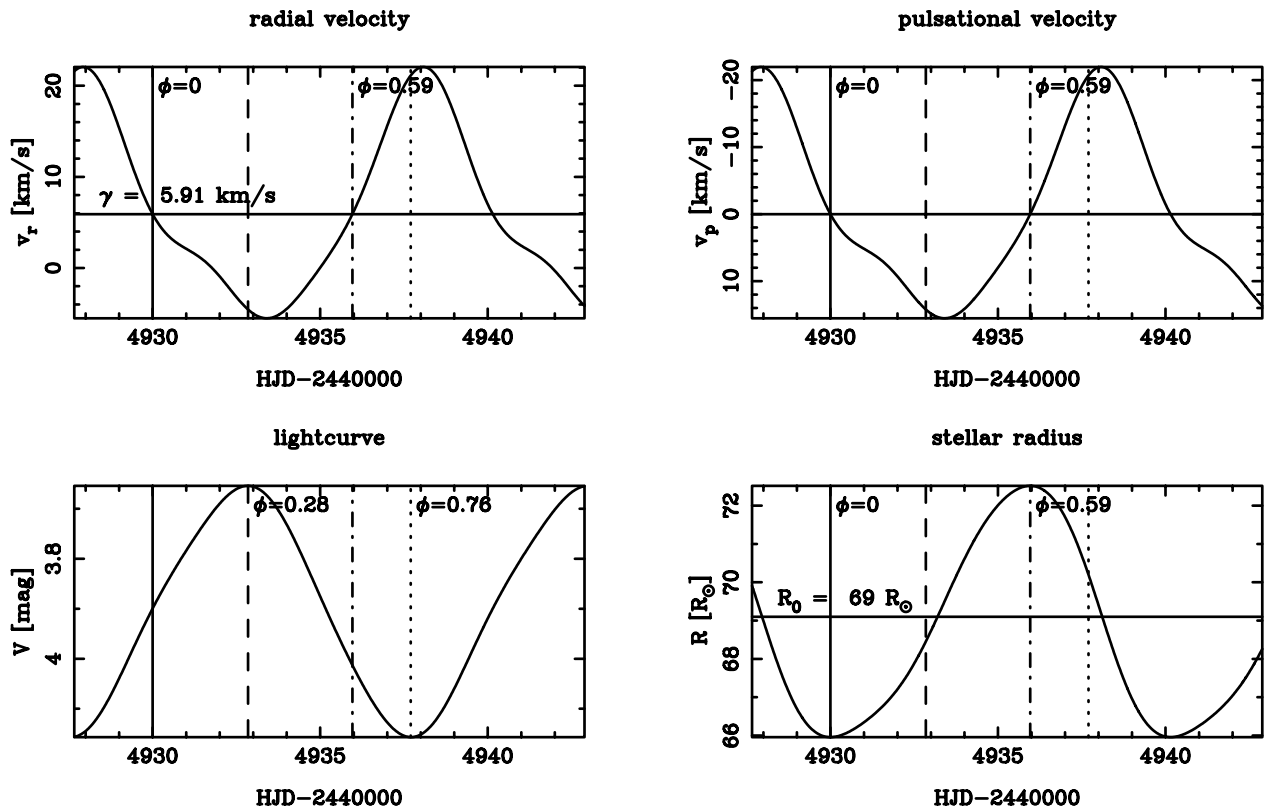


FIG. 1.—Comparison between radial velocity, pulsational velocity, light curve, and radius for ζ Gem, based on Bersier et al. (1994a, 1994b). The vertical solid line shows the pulsational velocity zero phase; the light-curve zero phase ($\phi \approx 0.28$) is indicated by the dashed line. Other important phases are maximum radius ($\phi \approx 0.59$, dot-dashed line) and minimum luminosity ($\phi \approx 0.76$, dotted line).

where γ is the systemic velocity taking into account the radial velocity of the star relative to the solar system, the minus sign inverts Doppler shifts into velocities relative to the Cepheid atmosphere, and p is the projection factor. The pulsational velocity of ζ Gem derived using equation (1) is plotted in Figure 1 (*top right panel*), using a constant projection factor of 1.36 (Burki, Mayor, & Benz 1982). The systemic velocity $\gamma = 5.91 \text{ km s}^{-1}$ was determined by requiring conservation of radius after the completion of one pulsational cycle and is consistent with the value of $6.5(\pm 1.0) \text{ km s}^{-1}$ derived by Wilson (1953) for the radial velocity of the star.

The zero phase in the velocity curve and in the subsequent discussion is set at the time in which v_p passes from negative to positive, e.g., when the star begins to expand after reaching the minimum radius. This point is marked in Figure 1 with a solid vertical line. In the case of ζ Gem, the maximum luminosity occurs at phase $\phi \approx 0.28$, which is 3 days after the zero-point phase (*dashed line*), given its 10.15 days period. Minimum luminosity is at $\phi \approx 0.76$ (*dotted line*), while maximum radius is at $\phi \approx 0.59$ (*dot-dashed line*).

The radius R is obtained by integrating the velocity v_p over time

$$R(t) = R_0 + \int_{t_0}^t v_p(t') dt', \quad (2)$$

where R_0 is the mean radius. An example is shown in Figure 1 (*bottom right*) for ζ Gem, which has $R_0 \approx 69 R_\odot$ (Krockenberger 1996).

Note, however, that the above expression is strictly correct only if v_p is associated with an individual mass

element in the stellar atmosphere. This is not the case for the photospheric line velocities (as the lines are produced by different photospheric layers during the stellar pulsation), nor for the velocity field of the hydrodynamic model (as the radial grid is not comoving with the atmosphere). This inconsistency, which translates in the nonconservation of the path integral in equation (2) over one pulsational period, should be taken into account in order to have a consistent reference frame for the observed and model velocities.

The condition of constant average radius for the pulsating atmosphere can, however, be achieved by adding an extra factor to the γ constant in equation (1). This was done implicitly when deriving the systemic velocity for ζ Gem. We did the same with the model pulsational velocity, deriving a correction factor of -0.475 km s^{-1} . With this condition, the model and observed v_p are directly comparable, allowing us to set the zero-point phase in the sequence of models.

The pulsational velocity of the hydrodynamic model was defined as the average velocity of the photospheric layers weighted over the region where the line formation occurs. This quantity, shown in Figure 2, is very similar to the observational v_p . Note the perturbation starting at $\phi \approx 0.9$, which is associated with a shock wave crossing the photosphere.

The bottom panel of Figure 2 shows the effective temperature of ζ Gem as a function of phase, derived by fitting the depth ratio of weak metallic lines as Fe I, Fe II, Si I, and a few other elements insensitive to the changes in metallicities (Krockenberger, Sasselov, & Noyes 1997). The effective

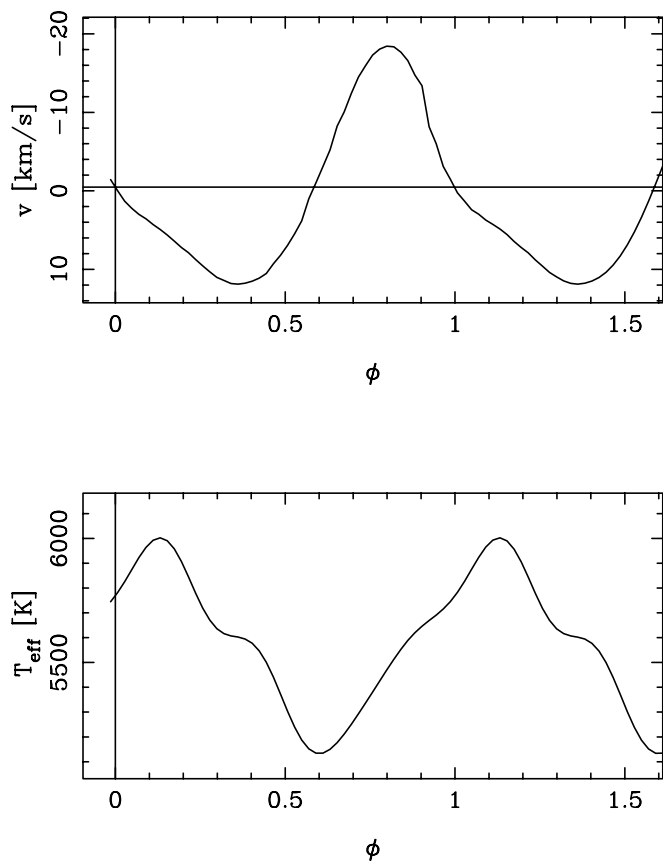


FIG. 2.—*Top*: Model pulsational velocity, obtained by averaging the velocities of the hydrodynamic model photospheric layers. *Bottom*: Stellar effective temperature of ζ Gem, derived as a function of phase by Krockenberger et al. (1997).

temperature here defined is the T_{eff} of the plane-parallel LTE atmosphere used to fit the observed line ratios. We will maintain this convention through the following discussion, since this quantity allows direct comparison between a model parameter and the observations.

The effective temperature plotted in Figure 2 is related to the luminosity curve of the Cepheid and is thus an important observable that we use to constrain our model intensity spectra, as explained in the following section.

2.3. Rosseland Opacities for Dynamic Atmospheres

The largest collection of stellar atomic and molecular opacities is available as part of the ATLAS9–12 numeric code (Kurucz 1970, 1979, 1993b), which incorporates no less than 58 million lines for different stellar metallicities and values of microturbulent velocity.

The Kurucz code initially computes static LTE model atmospheres in plane-parallel geometry and radiative equilibrium. The input parameters that define each model are the effective temperature T_{eff} , the gravity $\log g$, the convective mixing length L/H , the turbulent velocity V_{turb} , and the metallicity. The structure of a model atmosphere is evaluated on a radial grid in the mass coordinate $dM = \rho dr$. For each depth the model computes the local temperature, total pressure, electron density, Rosseland opacity, radiation pressure, and turbulent velocity (which is not allowed to change along the radial grid). The SYNTHE program, included in the ATLAS package, then allows the computa-

tion of intensity spectra $I_\nu(\lambda, \mu)$, from which limb-darkened profiles are derived.

In this work we adopted the ATLAS9 version of the Kurucz code, which incorporates a full treatment for line-blanketing; we do not expect that adopting ATLAS12 model atmospheres with opacity sampling would have produced significant differences in the atmospheric structure and resulting intensity profiles, at least in our wavelength range of interest (Kurucz, private communication).

Figure 3 shows the main differences between the snapshot of a dynamic atmosphere and a family of ATLAS9 models having $\log g$ from 0.5 to 2.0 and $T_{\text{eff}} \approx 5600$ K. The effective temperature for the static model has been chosen to match the observational estimate for the Cepheid T_{eff} at the same phase. Contrary to the hydrostatic case, the dynamic model shows a temperature inversion for $\log dM \lesssim 1.5$. This is due to the chromosphere attached to the Cepheid atmosphere, which is not reproduced by the static radiative equilibrium models. The deeper layers of the atmosphere, on the contrary, can be better approximated by hydrostatic equilibrium, with an appropriate choice in the $\log g$ parameter.

The agreement between the temperature distribution in the static and dynamic atmospheres, below the temperature inversion point, depends on how significant are the departures from hydrostatic and radiative equilibrium. A minor

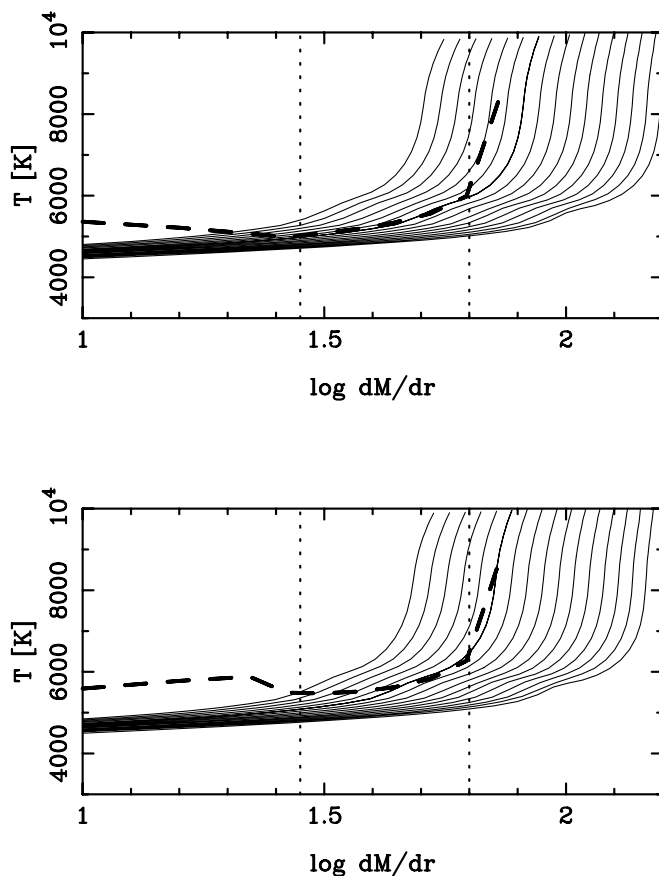


FIG. 3.—Thermal structure of ζ Gem models. The dashed lines are dynamic atmospheres computed at phase 0.4 and at phase 0.94 (*top and bottom, respectively*). Solid lines are hydrostatic models having the same T_{eff} as the hydrodynamic atmosphere, and $\log g$ from 0.5 to 2.0 in step of 0.1. Note the temperature inversion in the dynamic models, occurring for $\log dM/dr \approx 1.45$, and the shock wave crossing the atmosphere at phase 0.94 ($\log dM/dr \lesssim 1.3$). The fitting region used to match dynamic atmospheres with static models is marked by vertical dotted lines.

role is also played by departures from plane-parallel geometry. As shown in Sasselov & Lester (1994), however, spherical geometry becomes an important factor only for long-period Cepheids and can be neglected for our model of ζ Gem and the other short-period Cepheids that can be observed with the available interferometers.

Consider phase $\phi \simeq 0.40$ (Fig. 3, *top panel*), which is close to average radius, when the star is freely expanding. This is well after the effects of the shock wave (occurring at $\phi \simeq 0.9$) dissipated. The dynamic and static thermal structures are very similar, at least where the convective overshooting incorporated in ATLAS9 (absent in the dynamic models) is not important. The overshooting only affects the deepest layers in the stellar atmosphere and is responsible for the lower temperature gradient in the hydrostatic temperature profile.

At other phases (e.g., for $\phi \simeq 0.94$), the hydrodynamic effects (the shock wave in particular) are stronger, causing a larger departure from hydrostatic equilibrium. (Fig. 3, *bottom panel*). The spread in the temperature distribution in this case can be large, and a single hydrostatic model that is a good approximation of the hydrodynamic atmosphere cannot be identified.

In a typical Cepheid atmosphere, the contribution function for the photospheric lines is negligible in both the chromosphere and in the deep layers subjected to convective overshooting, as shown in Sabbey et al. (1995). In fact, the region where the hydrodynamic thermal structure is best approximated by an equivalent hydrostatic atmosphere is precisely where the photospheric contribution functions are at maximum. Our assumption is that the opacities computed in hydrostatic equilibrium in this region can be used to compute emergent spectral intensities with the dynamic model.

On this basis, we fit our dynamic model for ζ Gem with a grid of ATLAS atmospheres having $V_{\text{turb}} = 4 \text{ km s}^{-1}$ and $\log g$ from 0.5 to 2.0 in steps of 0.1. Since the effective temperature for our hydrodynamic models is not well defined, we have set the ATLAS fitting grid to the T_{eff} value determined by Krockenberger et al. (1997) for each pulsational phase. The fit was done by minimizing the normalized χ^2 , computed on the “fitting region” in which the contribution functions are at maximum, between each dynamic model and all static atmospheres in the ATLAS grid. This technique allows us to find the best match between the dynamic models and the static atmospheres, even in the cases in which the dynamic model temperature structure cuts across several static models (as shown in Fig. 3 for $\phi = 0.94$). The result is a family of static atmospheres, each having a Rosseland opacity computed with the full set of relevant atomic species, to be used instead of the unknown opacities for the dynamic models. The error associated with this procedure can be visualized as the separation between the opacities of two consecutive models in the fitting grid, which is $\lesssim \pm 0.3$ in the logarithmic scale (see Fig. 4).

Note that once the best-fit static model is determined for each phase, it is the whole atmospheric thermodynamic status that is constrained, e.g., not only the temperature distribution T , but also the electron density x_{ne} and the pressure P . Differences in the x_{ne} and P distributions between static and dynamic models are to be expected, given the different equation of state used in the two cases. These inconsistencies reflect in the accuracy of the Rosseland opacity adopted for the dynamic atmosphere,

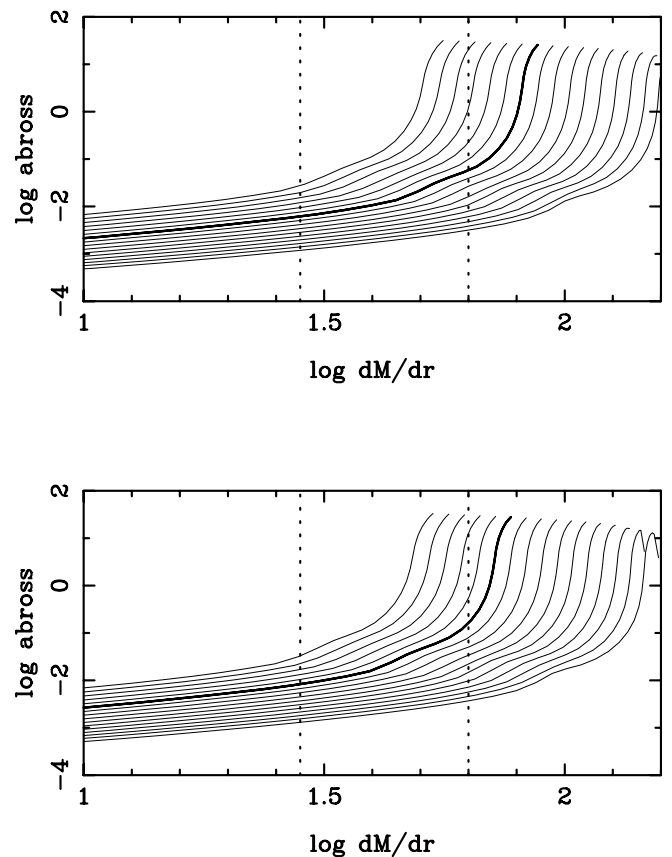


FIG. 4.—Rosseland opacities for dynamic models at $\phi \simeq 0.4$ and $\phi \simeq 0.94$ (*top and bottom, respectively*). The thick solid line is the Rosseland opacity of the static model providing the best fit to the hydrodynamic atmosphere; the thin lines are the opacities for other static models having the same T_{eff} and different $\log g$. Given the uncertainty in the determination of the best-fit $\log g$, the resulting error in the Rosseland opacity can be visualized as the two curves bracketing the best-fit opacity. This is $\lesssim \pm 0.3$ in the fitting region (*vertical dotted lines*).

which is computed with the pressure and electron density relative to the hydrostatic case.

2.4. Intensities and Limb Profiles

The spectral intensity distribution for each phase of our dynamic atmospheres are finally computed by adapting SYNTHE/ATLAS to process our hybrid models, which combine the hydrodynamic atmospheres with hydrostatic Rosseland opacities.

Each hybrid model is characterized by the following parameters:

1. T_{eff} is the effective temperature of the best-fit ATLAS model, which was set to the value derived by Krockenberger et al. (1997);
2. $\log g$ determined by the best fit of the dynamic model with the static grid;
3. V_{turb} , L/H , metallicity and Rosseland opacities taken from the best-fit hydrostatic model;
4. T , x_{ne} , and P obtained by splicing the hydrodynamic model (below the temperature inversion point) with the static model (above T inversion, e.g., effectively removing the chromosphere).

The removal of the chromosphere is necessary, because SYNTHE is in essence a radiative equilibrium code and cannot treat temperature inversions and discontinuities in

the radial grid. This step is justified, as noted before, by the consideration that the only part of the atmosphere relevant in the photospheric emission is where the contribution function is maximum. This is the same region used in § 2.3 to perform the fitting between static and dynamic atmospheres. Eventual discontinuities around the temperature inversion point in the two segments of the T , x_{ne} , and P profiles have been eliminated by rescaling the static part with a suitable normalization factor.

An example of final temperature, electron density, and pressure radial profiles of our ζ Gem model is shown in Figure 5 for two representative phases. At $\phi \simeq 0.40$, the T and x_{ne} dynamic model distributions closely match their hydrostatic approximation, at least in the region used for the fit (*vertical dotted lines*). The pressure of the dynamic atmosphere, on the contrary, is lower than the static equivalent, reflecting the change in the equation of state. At phase 0.94, the extra energy dissipated by the traveling shock wave is responsible for an increase in the dynamic model electron density and pressure, which becomes higher than in the hydrostatic atmosphere with the same temperature profile. The increased electron density of the hybrid model, reflecting the structure of the hydrodynamic atmosphere, is in part responsible for the different limb profile of the Cepheid at this phase.

The spectral intensity distributions (and the associated limb profiles) are then computed (together with a consistent set of molecular opacities) by running SYNTHE on the hybrid models. The results are discussed in the following section.

3. DISCUSSION

Limb profiles for our model Cepheid are obtained by plotting the intensity $I_\nu(\lambda, \mu)$ as a function of the projected radial coordinate $\sin \alpha$ (where α is the angle between the line of sight and the direction of the emergent flux, and $\mu = \cos \alpha$). Given the detailed treatment of stellar opacities in our computation, the profiles thus obtained can be trusted analyzing the wavelength dependence of limb darkening. Also, the explicit time dependence of our dynamic models allows us to follow the variations in the limb profile as the Cepheid star pulsates.

3.1. Differences between Static and Dynamic Models

Figure 6 compares static and dynamic models at three representative phases. At $\phi \simeq 0.4$ the limb-darkening profiles computed with the hydrodynamic models are very similar to the hydrostatic equivalent. This is not surprising, since at this phase the atmosphere is quasistatic, having long dissipated the transient hydrodynamic effects caused by the passing shock wave. Even though the pressure is very different in the static and dynamic case, the spectral emission (and thus the limb darkening) is similar, confirming that T and x_{ne} are the main parameters constraining the photospheric emission. This is an important validation of the procedure described in § 2.

Dramatic evidence that the limb darkening is substantially affected by the hydrodynamic effects is given in the two lower panels of Figure 6. The two panels compare the static and dynamic limb profiles at $\phi \simeq 0.92$ (shock wave

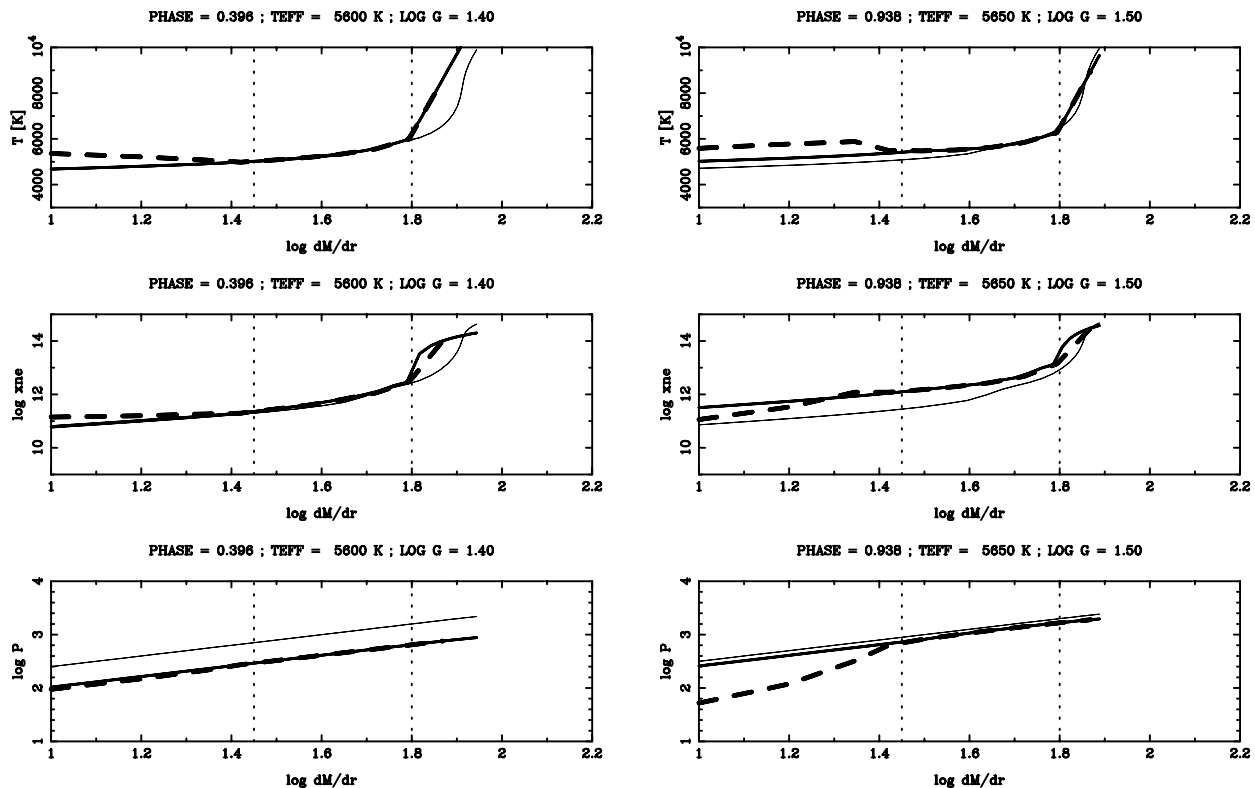


FIG. 5.—Temperature, electron density, and pressure of model atmospheres at $\phi \simeq 0.4$ and $\phi \simeq 0.94$ (*left and right, respectively*). The dashed lines are the original hydrodynamic models, and the thin solid lines their best-fit hydrostatic atmospheres. The thick solid lines are the spliced hybrid models obtained as explained in § 2.4. Note that, at $\phi \simeq 0.4$, the T and x_{ne} distributions of static and dynamic models are very similar, at least in the fitting region (enclosed between the vertical dotted lines). The pressure, on the contrary, is larger, owing to the different equation of state in the two models. The opposite is true at $\phi \simeq 0.94$ because of the passage of the shock wave, which excites the atmosphere increasing x_{ne} with respect to the hydrostatic equivalent.

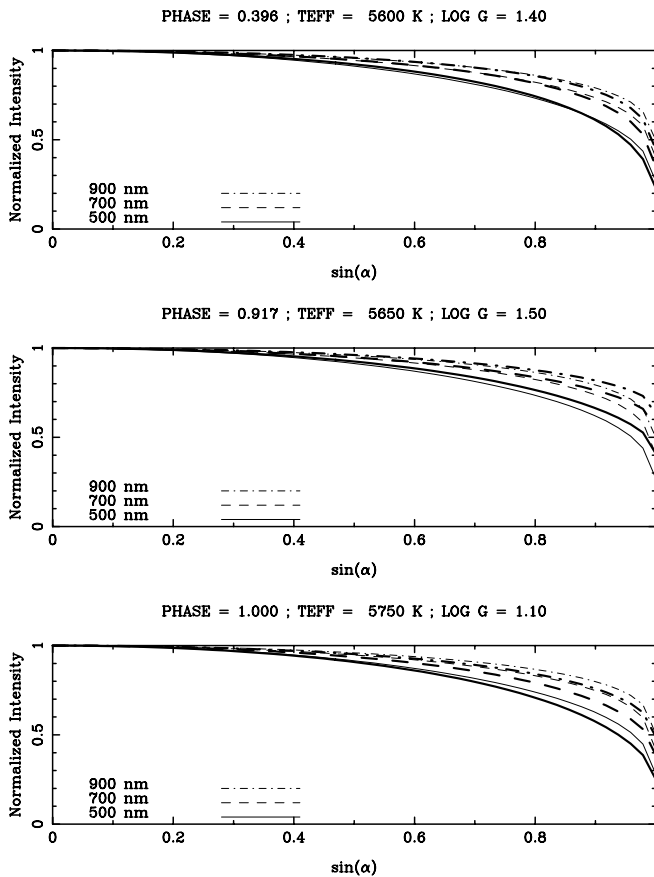


FIG. 6.—Monochromatic limb profiles computed at 500, 700, and 900 nm for $\phi \simeq 0.4, 0.92,$ and $1,$ respectively. Note that the low spectral resolution of our intensity distributions is similar to the spectral resolution of the actual Navy Prototype Optical Interferometer observations. Thick lines are profiles for the hydrodynamic model; thin lines are computed for a hydrostatic atmosphere having the same T_{eff} and $\log g.$

crossing the photosphere) and at $\phi \simeq 1$ (minimum radius). In the first case the newborn shock wave reduces ∇T with respect to the hydrostatic atmosphere, and the limb darkening is lower. At minimum radius the effects of the shock wave have dissipated, and the compression of the atmosphere gives rise to a larger temperature gradient. This is responsible for a larger limb darkening. In both cases the changes in the amount of limb darkening with respect to the static model is mostly visible at shorter wavelengths, where the opacity is lower and the limb darkening larger.

3.2. Changes of Limb Darkening with Phase and Wavelength

Figure 7 puts in evidence the full amount of monochromatic limb profile variations as a function of phase, for $\lambda = 500$ nm. As explained before, the limb darkening for our model of ζ Gem is greater at minimum radius and lower when the shock wave is crossing the photosphere.

The effect of phase on the limb profiles is not only restricted to the amount of limb darkening but is also reflected in the shape of the profile itself. Consider the two profiles for $\phi \simeq 0.76$ and $\phi \simeq 0.91.$ Despite the small difference in phase, they cross each other at $\sin \alpha \simeq 0.75,$ which indicates that the gradient of I_v with respect of $\sin \alpha$ is also a function of the pulsational phase. This example highlights the intrinsic limits in the parameterization of the limb profiles that result from a single limb-darkening parameter.

A closer examination of Figure 6 shows that even when the dynamic atmosphere is close to hydrostatic equilibrium ($\phi \simeq 0.4$), static models are slightly less darkened for $\sin \alpha \lesssim 0.85$ and more darkened on the limb. Even in the most favorable phases, the dynamic limb profiles cannot be obtained by scaling suitable profiles computed with a static atmosphere. This is a direct consequence of the similar difficulties, mentioned in § 2.3, of fitting the hydrodynamic thermal structure with a single hydrostatic model. Again, the different functional shape between the static and

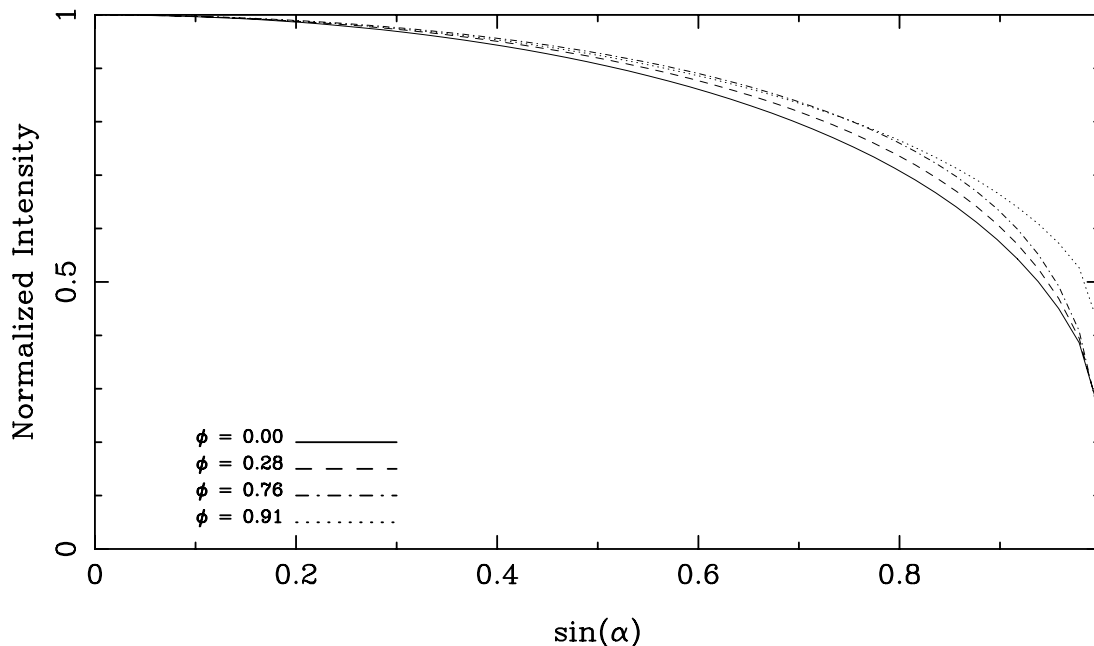


FIG. 7.—Decreasing limb-darkened profiles at phases 0 (minimum radius), 0.28 (maximum luminosity), 0.76 (minimum luminosity), and 0.91 (passage of the shock wave through the photosphere). The profiles are computed for $\lambda = 500$ nm.

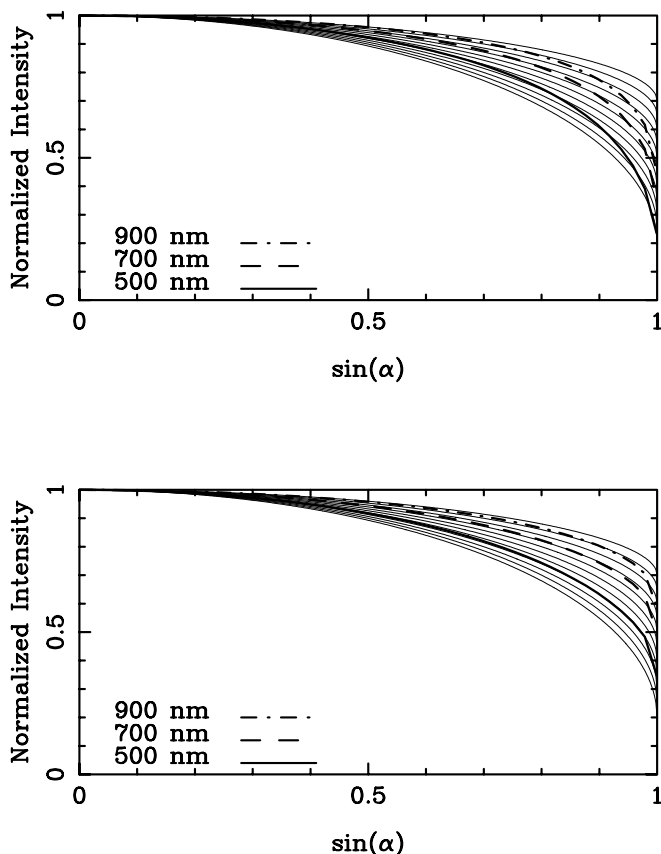


FIG. 8.—Different levels of limb darkening at phase 0.4 (*top*) and 0.94 (*bottom*) for $\lambda = 500, 700,$ and $900 \mu\text{m}$ (*thick lines*). Curves with linear limb darkening $I_v(\mu) = I_v(1)[1 - u(1 - \mu)]$, with u from 0.3 to 0.80, are plotted for reference (*thin lines*).

dynamic profiles depends strongly on the phase and the wavelength and requires detailed modeling.

As expected, our limb profiles have larger darkening at shorter wavelengths. This is mainly a consequence of the source function and the optical depth dependence on wavelength. At 900 nm and in the near-IR, different lines of sight along the stellar disk probe regions of the stellar atmosphere where the source function is similar. This results in a flat limb intensity profile and thus low limb darkening. At 500 nm the source function in the atmospheric layers probed by the different directions change more rapidly toward the limb, producing a larger limb darkening. This effect is even larger when going to shorter wavelengths in the UV (300–400 nm).

This wavelength dependence of limb darkening is also affected by phase-dependent hydrodynamic effects. Figure 8 presents limb profiles for $\lambda = 500, 700,$ and 900 nm at two different phases. As shown in the figure, the limb profiles derived for dynamic atmospheres are in most cases very different from those computed using static models, or from linear limb-darkening curves (Milne 1921).

4. CONCLUSIONS

The increasing amount of available interferometric data requires accurate stellar models to convert the raw visibil-

ities into meaningful angular diameters. This is particularly true in the case of Cepheids, whose radial pulsations add another degree of complexity in modeling their spectral emission. The Cepheid variability is being used as a means to accurately determine their distance and thus the scale of the entire universe; at the same time there is a tendency to neglect their pulsations when computing the properties of their atmospheres, as they change during the Cepheid luminosity cycle.

We presented here a new approach that is used to derive time-dependent center-to-limb brightness distributions for classical Cepheids. The adoption of second-order accurate hydrodynamic calculations in spherical geometry, and the inclusions of a complete set of atomic and molecular opacities, improve our limb-darkening profiles over previous computations. Conventional limb-darkened interferometric measurements are done by adopting a suitable stellar model having the same spectral type and average T_{eff} of the Cepheid (see, e.g., Nordgren et al. 1999). In the past, however, none of the available models, has been specifically computed for a Cepheid, and the variations of T_{eff} and $\log g$ as the star pulsates are usually not taken into account (the case of $\log g$ is particularly dire, given the difficulty of a precise measurement of this parameter, and T_{eff} may suffer from the ambiguities in its definition).

These limitations are absent in our models, which can be computed for individual Cepheids; the only requirements are an accurate model for the pulsational piston (see Buchler, Moskalik, & Kovacs 1990) and the temporal variation of T_{eff} . Both conditions can be satisfied for most of the nearby Cepheids and constrained with available high-resolution spectral observations.

The main differences between our dynamic models and conventional static limb-darkening profiles are analyzed in detail in the previous section. However, it is important to remark once more that the amount of limb darkening between static and dynamic models is significantly different and can be either larger or smaller according to the pulsational phase. The actual shape of the limb profile is also a function of phase and cannot be reproduced by a single family of static models or a single limb-darkening parameter.

These results highlight the importance of hydrodynamic calculations in the determination of center-to-limb brightness distribution for pulsating Cepheids. In a future paper we will demonstrate that the effects here described are already measurable with the current interferometric technology and affect the determination of Cepheid angular diameters. This issue is becoming very important when measuring the variations of such diameters as the star pulsates, which is the first step to provide a reliable determination of its distance through the geometric Baade-Wesselink method.

We wish to thank Bob Kurucz for valuable discussions and the anonymous referee for comments that helped us to improve the paper. This work was partially supported by NSF grant AST 98-76734. M. K. is a member of the *Chandra* Science Center, which is operated under contract NAS 8-39073 and is partially supported by NASA.

REFERENCES

- Baade, W. 1926, *Astron. Nachr.*, 228, 359
 Bersier, D., Burki, G., & Burnet, M. 1994a, *A&AS*, 108, 9
 Bersier, D., Burki, G., Mayor, M., & Duquennoy, A. 1994b, *A&AS*, 108, 25
 Buchler, J. R., Moskalik, P., & Kovacs, G. 1990, *ApJ*, 351, 617
 Burki, G., Mayor, M., & Benz, W. 1982, *A&A*, 109, 258
 Claret, A., Díaz-Cordovéz, J., & Giménez, A. 1995, *A&AS*, 114, 247
 Cuntz, M. 1987, *A&A*, 188, L5
 Feast, M. W., & Catchpole, R. M. 1997, *MNRAS*, 286, L1
 Fieldus, M. S., & Lester, J. B. 1990, in *ASP Conf. Ser. 9, 6th Cambridge Workshop on Cool Stars, Stellar Systems, and the Sun*, ed. C. Wallerstein (San Francisco: ASP), 76
 Freedman, W. L., et al. 2001, *ApJ*, 553, 47
 Horner, S., et al. 2000, *BAAS*, 197, 1404
 Karp, A. 1975, *ApJ*, 201, 641
 Krockenberger, M. 1996, Ph.D. thesis, Harvard Univ.
 Krockenberger, M., Sasselov, D., & Noyes, R. W. 1997, *ApJ*, 479, 875
 Kurucz, R. L. 1970, *SAO Special Rep.* 309
 ———. 1979, *ApJS*, 40, 1
 ———. 1993a, in *Light-Curve Modeling of Eclipsing Binary Stars*, ed. E. F. Milone (New York: Springer), 93
 ———. 1993b, CD-ROM 13, *ATLAS9 Stellar Atmosphere Programs and 2 km/s Grid* (Cambridge: SAO)
 Lane, B. F., Kuchner, M. J., Boden, A. F., Creech-Eakman, M., & Kulkarni, S. R. 2000, *Nature*, 407, L485
 Leavitt, H. S. 1906, *Ann. Astron. Harvard Coll. Obs.*, 60, 87
 Madore, B. F., & Freedman, W. L. 1998, *ApJ*, 492, 110
 Manduca, A. 1979, *A&AS*, 36, 411
 Manduca, A., Bell, R. A., & Gustafsson, B. 1977, *A&A*, 61, 809
 Milne, E. A. 1921, *MNRAS*, 81, 361
 Nordgren, T. E., et al. 1999, *AJ*, 118, 3032
 Parsons, S. B. 1971, *ApJ*, 164, 355
 Sabbey, C. N., Sasselov, D. D., Fieldus, M. S., Lester, J. B., Venn, K. A., & Butler, R. P. 1995, *ApJ*, 446, 250
 Sasselov, D. D., & Karovska, M. 1994, *ApJ*, 432, 367
 Sasselov, D. D., & Lester, J. B. 1994, *ApJ*, 423, 795
 Sasselov, D. D., & Raga, A. 1992, in *ASP Conf. Proc. 26, 7th Cambridge Workshop on Cool Stars, Stellar Systems, and the Sun*, ed. M. Giampa & J. Bookbinder (San Francisco: ASP), 549
 Wesselink, A. 1946, *Bull. Astron. Inst. Netherlands*, 10, 91
 Willson, L. A., & Bowen, G. W. 1985, in *Relations between Chromospheric-Coronal heating and Mass Loss in Stars*, ed. R. Stalio & J. B. Zirker (Trieste: Osservatorio Astronomico di Trieste), 127
 Wilson, R. E. 1953, *Gen. Cat. of Stellar Radial Velocities*, Carnegie Inst. Washington Publ. 601